Universiteit Antwerpen

Ambient and high pressure CuNiSb₂ : metal-ordered and metal-disordered NiAs-type derivative pnictides

uantwerpen.be

Ambient and High Pressure CuNiSb₂: Metal-Ordered and Metal-Disordered NiAs-Type Derivative Pnictides

Callista M. Skaggs,[1] Chang-Jong Kang,[2,#] Christopher J. Perez,[3] Joke Hadermann,[4] Thomas J. Emge,[5] Corey E. Frank,[5] Chongin Pak,[6] Saul H. Lapidus,[7] David Walker,[8] Gabriel Kotliar,[2] Susan M. Kauzlarich,[3] Xiaoyan Tan,*[1,5] and Martha Greenblatt*[5]

[1]Department of Chemistry and Biochemistry, George Mason University, Fairfax, Virginia, 22030, United States

[2]Department of Physics and Astronomy, Rutgers, The State University of New Jersey, Piscataway, New Jersey, 08854, United States

[3] Department of Chemistry, University of California, Davis, California, 95616, United States

[4] EMAT, University of Antwerp, Groenenborgerlaan 171, B-2020 Antwerp, Belgium

[5]Department of Chemistry and Chemical Biology, Rutgers, The State University of New Jersey, Piscataway, New Jersey, 08854, United States

[6]Department of Chemistry and Biochemistry, Florida State University, Tallahassee, Florida, 32306, United States

[7]Advanced Photon Source, Argonne National Laboratory, Argonne, Illinois, 60439, United States

[8]Lamont Doherty Earth Observatory, Columbia University, Palisades, New York, 10964, United States

ABSTRACT

The mineral Zlatogorite, CuNiSb₂, was synthesized in the laboratory for the first time by annealing elements at ambient pressure (CuNiSb₂-AP). Rietveld refinement of synchrotron powder X-ray diffraction data indicates that CuNiSb₂-AP crystallizes in the NiAs-derived structure ($P\bar{3}m1$, #164) with Cu and Ni ordering. The structure consists of alternate NiSb₆ and CuSb₆ octahedral layers via face-sharing. The formation of such structure instead of metal disordered NiAs-type structure ($P6_3/mmc$, #194) is validated by the lower energy of the ordered phase by first-principle calculations. Interatomic crystal orbital Hamilton population, electron localization function, and charge density analysis reveal strong Ni-Sb, Cu-Sb, and Cu-Ni bonding, and long weak Sb-Sb interactions in CuNiSb₂-AP. The magnetic measurement indicates that CuNiSb₂-AP is Pauli paramagnetic. First-principle calculations and experimental electrical resistivity measurements reveal that CuNiSb₂-AP is a metal. The low Seebeck coefficient and large thermal conductivity suggest that CuNiSb₂ is not a potential thermoelectric material. Single crystals were grown by chemical vapor transport. The high pressure sample (CuNiSb₂-8GPa) was prepared by pressing CuNiSb₂-AP at 700 °C and 8 GPa. However, the structure of single crystal and CuNiSb₂-8GPa is best fit with a disordered metal structure in the $P\bar{3}m1$ space group, corroborated by transmission electron microscopy.

INTRODUCTION

The hexagonal NiAs structure ($P6_3/mmc$, #194) is one of the common structures that accommodate a large number of intermetallic compounds such as binary TX and ternary TT′X₂ (T = transition metal, X = nonmetal) compounds with disordered T and T′ atoms occupying the same site.[1] When the two metals located in the structure have large size or charge difference, they can become ordered and form a derived-trigonal '112' structure ATX₂ (A = alkali metal, Ag, Cu, Cd, Tl; T = transition metal, Tl, In, Sn, Bi; X = nonmetal) with $P\bar{3}m1$ space group. In the hexagonal NiAs ($P6_3/mmc$) structure, As atoms are hexagonal close-packed with Ni atoms occupying all the octahedral sites. The structure can be viewed as layered face-sharing NiAs₆ octahedral sheets stacking along the crystallographic c axis (Figure 1a). When NiAs₆ octahedra are replaced with alternate AX₆ and TX₆ octahedral layers, a metal-

ordered NiAs-derived trigonal structure forms. The reported examples of '112' structures are mainly chalcogenides, such as, $LiCrQ_2$ (Q = S, Se, Te),[2,3,4] $LiTiS_2$,[5] $LiVS_2$,[3] $LiSnS_2$,[6] $NaCrTe_2$,[4] $CdTlQ_2$ (Q = S, Se, Te),[7,8] $CdInS_2$,[9] $TlCrTe_2$,[10,11] $CuRTe_2$ and $CuRSe_2$ (R = rare-earth metal),[12,13] $AgTmTe_2$,[14] $AgScSe_2$,[15] and $AgBiQ_2$ (Q = S, Se, Te).[16] Among those, $CuTmTe_2$,[17] $AgTmTe_2$,[18] and $AgBiSe_2$,[19,20,21] are experimentally established good thermoelectric materials. First-principles calculations also predicted other related '112' (such as $YAgTe_2$, $YCuTe_2$) compounds as promising thermoelectric materials.[22]

In addition to the reported chalcogenides, this metal-ordered NiAs-derived structure has also been observed in other '112' intermetallic compounds. $AuCuSn_2$ and $AuNiSn_2$ are two examples of stannides in which Au and Cu/Ni have different atom sizes.[23,24] In terms of pnictides, an experimental compound $HfMnSb_2$ was reported in 2016.[25] It is not surprising that Hf and Mn atoms are ordered due to the large size difference. This is an interesting compound that exhibits conical spin order due to Mn layers. The first '112' pnictide, however, should be the mineral compound $CuNiSb_2$ which was reported in 1994,[26] and named as Zlatogorite later based on its origin from Zolotaya Gora deposit in the Central Urals.[27]

The mineral compound $CuNiSb_2$ caught our attention, because it is uncommon that similar covalent radii of Cu (r =1.32Å) and Ni (r =1.24Å)[28] atoms could stabilize this metal-ordered NiAs-derived structure, while the reported examples of such '112' intermetallics in the Pearson handbook contain metals with a significant size difference.[1] In contrast, $MnCrSb_2$, $MnNiSb_2$, and $CrNiSb_2$ crystallize in the NiAs-type structure, in which $3d$ transition metals are disordered.[29,30,31] Although $MnCrSb_2$ can be prepared by a solid-state method easily, $MnNiSb_2$ can only be formed at high pressure.[31] $CuNiSb_2$ has only been found in nature and was yet to be synthesized in the laboratory. Therefore, it was of interest to study if $CuNiSb_2$ could be made at ambient pressure or high pressure, and whether or not high pressure would affect the metal-ordered or metal-disordered NiAs-derived structure. In addition, the physical properties of $CuNiSb_2$ are worthy of being studied because many related layered nominal '112' pnictides exhibit exotic physical properties. For instance, $LaAgSb_2$ and $LaAuSb_2$ ($P4/nmm$) exhibit charge density wave,[32,33] $SrZnSb_2$ ($Pnma$) shows larger magnetoresistance and magnetothermopower,[34] and $AMnBi_2$ (A = Ca, Sr, Ba, or rare earth elements, $P4/nmm$) are topological materials.[35]

In this manuscript, we report the synthesis, electronic structure, and physical properties of $CuNiSb_2$ for the first time. Polycrystalline samples can be prepared at ambient pressure with a two-step solid-state annealing process. The crystal structure and composition have been confirmed by high-intensity synchrotron X-ray diffraction and elemental analysis. Density functional theory calculations have been carried out to understand the electronic structure, bonding, and reveal the energy difference between the metal-ordered and metal-disordered NiAs structures. High pressure (8 GPa) was also applied to the crystal structure to investigate a possible structural transition.

EXPERIMENTAL SECTION

Starting Materials and Synthesis. $CuNiSb_2$ polycrystalline samples were synthesized at ambient pressure ($CuNiSb_2$ –AP) with the solid-state method in two steps. Copper (99.999 wt.%, Alfa Aesar), nickel (99.996 wt.%, Alfa Aesar), and antimony (99.999 wt.%, Alfa Aesar) powders were mixed and ground in stoichiometric amounts inside of an argon-filled glove box with a low concentration of O_2

and H_2O (< 1 ppm). The thoroughly ground elements were pressed into a pellet and transferred into a quartz tube (O.D = 9.5 mm), which was sealed under vacuum (< 10^{-2} mbar). The ampule was first slowly heated to 800 °C in 2 days, held at this temperature for 7 days, and cooled to room temperature in 6 hours. This treatment turned the pellet into a shinning metallic ball. The ball was then ground, pelletized, and again sealed in a quartz tube. The ampule was heated to 650 °C within 1 day, held at this temperature for 7 days, and then cooled over the course of 6 hours. The obtained black pellet was ground and characterized by powder X-ray diffraction. The chemical vapor transport method was used to grow single crystals of $CuNiSb_2$. $CuNiSb_2$ polycrystalline powder and $AlCl_3$ as a transport reagent were sealed in a quartz tube (O.D = 12.5 mm) and heated in a three-zone horizontal furnace. The source temperature and crystal growth zone temperatures were set at 800 and 765 °C, respectively. Tiny crystals (< 0.1mm) were grown after being held at the programed heating profile for 2 weeks.

High Pressure Sample. $CuNiSb_2$-AP powders were packed into an open-ended Al_2O_3 crucible, which was transferred into a 6mm, finned, 646 ceramic octahedron module monitored and controlled with type D W3Re/W25Re thermocouple wires.[36] The octahedron module was then assembled with eight truncated tungsten carbide cubes, and loaded into the Walker-type multi-anvil high pressure press. The pressure was increased to 8 GPa overnight. Once the pressure reached the programed pressure (8 GPa), the sample was heated quickly from room temperature to 700 °C, and held for 1 hour, and then quenched to 25 °C in a few minutes. The obtained high pressure sample ($CuNiSb_2$-8GPa) was a dense black metallic pellet.

Laboratory and Synchrotron Powder X-ray Diffraction. Powder X-ray diffraction (PXD) patterns of polycrystalline samples were collected at room temperature for 30 mins with the 2θ range from 10 to 70° on a Bruker D8 Advance Diffractometer (Cu Kα, λ =1.5418 Å) with an SOL-X solid-state detector. Room-temperature synchrotron powder X-ray diffraction (SPXD) patterns were collected ($0.5° < 2\theta < 50°$) on both $CuNiSb_2$-AP and $CuNiSb_2$-8GPa samples at the 11-BM beamline at the Advanced Photon Source, Argonne National Laboratory. Rietveld refinements of the SPXD data were carried out with the suite of FullProf programs.[38]

Single Crystal X-ray Diffraction. Single crystal X-ray data were recorded at 150 K on a Bruker Smart diffractometer with an APEX CCD detector and graphite-monochromatized Mo Ka radiation. The data were corrected for absorption (numerical type) with Bruker SAINT software (SADABS method).[37] The 150 K crystal structure of $CuNiSb_2$ was solved with the known $P\bar{3}m1$ phase,[26] and refined with SHELXL (2018) program.[38] The details of structure refinement are provided in Tables 1 and 2 below, and SI Tables S1 and S2.

Chemical Analysis. Elemental analyses of $CuNiSb_2$-AP polycrystalline samples were carried out with a Zeiss-Sigma Field Emission Scanning Electron Microscope (SEM) with Oxford INCAEnergy 250 Energy Dispersive X-ray spectroscopy (EDX) microanalysis system.

Thermogravimetric Analysis (**TGA**) **and Differential Scanning Calorimetry (DSC).** TGA and DSC data were collected on $CuNiSb_2$-AP with an SDT Q600 TA Instrument. About 25 mg polycrystalline samples were heated inside an alumina crucible from 25 to 1000 °C at a heating and cooling rate of 10 °C/min under argon flow. After the measurement, the remaining samples were analyzed by PXD.

Physical Properties. Magnetic properties were measured on $CuNiSb_2$-AP polycrystalline samples with a Quantum Design superconducting quantum interference device (SQUID) MPMS-XL magnetometer. Field-cooled (FC) magnetic susceptibility was recorded between 1.8 and 300 K in a direct-current applied field of 1 T. The sample was measured without a sample holder and sealed directly inside the straw. A Dr. Sinter Lab Jr. SPS-211Lx spark plasma sintering (SPS) system (Sumitomo, Tokyo, Japan) was used to consolidate the bulk powder sample (about 0.5 g) into a dense pellet in a 4 mm high-density graphite die (POCO) under vacuum (< 10 Pa). The sample was pressed at 550 °C for 15 mins with the applied pressure of 3 kN. The geometric sample density was larger than 91% of the theoretical density. The resulting black disk (4 mm diameter, 1.5 mm thick) was polished flat and attached between two gold plated copper leads with silver conductive epoxy. The epoxy was cured in a vacuum oven at 150 °C for two hours and allowed to cool under vacuum overnight. Thermoelectric properties were measured (2 K ~ 300K) with a PPMS (Physical Property Measurement System) using the thermal transport option (TTO).

Transmission Electron Microscopy (TEM). Both $CuNiSb_2$-AP and $CuNiSb_2$-8GPa samples were analyzed with TEM. Ground fine powders were mixed with ethanol in an ultrasonic bath. The obtained suspension was then deposited onto a holey TEM grid covered with carbon. Electron diffraction (ED) patterns of both samples were acquired with a Phillips CM20 microscope operated at 200 kV.

First Principle Calculations. Density functional theory (DFT) was used to investigate the electronic structure. Structural parameters were taken from SPXD refinements. To study the stable type of crystal structure, the virtual crystal approximation (VCA) method,[39] which is implemented in the Quantum Espresso code,[40,41] was employed within the optimized norm-conserving Vanderbilt pseudopotential.[42] The kinetic energy cutoffs for wave functions and charge density were chosen to be 40 and 160 Ry, respectively, in the VCA calculations. After the stable crystal structure was found through the VCA calculations, electronic structures including the density of states (DOS), electron localization function (ELF), and charge density distribution were obtained using the projector augmented wave method as implemented in the Vienna *ab initio* simulation package (VASP).[43,44,45,46] An 11×11×8 k-point mesh was used for the Brillouin zone integration. A plane-wave cutoff of 520 eV and the generalized gradient approximation of Perdew-Burke-Ernzerhof (PBE) was used.[47] The full-potential linearized augmented plane-wave method implemented in WIEN2k was also employed to double-check the electronic structures.[48] The interatomic crystal orbital Hamilton population (COHP) analysis of $CuNiSb_2$-AP was performed with the tight binding-linear muffin tin orbitals-atomic sphere approximation (TB-LMTO-ASA) software package.[49] Calculations of $CuNiSb_2$-AP containing a basis set of Cu-4s/4p/3d, Ni-4s/4p/3d/, Sb-5s/5p/4d were carried out with space group $P\bar{3}m1$ after converging the total energy on a dense of 24×24×16 mesh with 885 irreducible k-points.

RESULTS AND DISCUSSION

Synthesis and Crystal Structure. Based on the literature reports on the synthesis of $MnNiSb_2$ and $Mn_{1-x}Ni_xSb$ (0 < x < 1) at high pressure with MnSb and NiSb,[31] and $MnCrSb_2$ at ambient pressure from the elements,[29] we planned to start the synthesis of $CuNiSb_2$ with the two binary pnictides: CuSb and NiSb, but CuSb is absent in the Cu-Sb phase diagram.[50] Therefore, polycrystalline samples of $CuNiSb_2$ were

prepared by mixing elements in the stoichiometric ratio in a vacuum quartz ampule. After the first step of annealing the ampule at 800 °C for a week, a melted ball with metallic shinning color was obtained. PXD data indicate that the product is a mixture of $CuNiSb_2$, Cu_2Sb, NiSb, and Sb (Figure S1). Based on the balanced equation: $Cu_2Sb + 2NiSb + Sb = 2CuNiSb_2$, this mixture was then annealed at 650 °C for 7 days to obtain the target phase. Phase-pure samples (Figure 2) were successfully formed at ambient pressure, which is a much simpler method in comparison to the high-pressure process required for the formation of $MnNiSb_2$. These results reveal that the reported mineral Zlatogorite, $CuNiSb_2$, can be prepared in the laboratory. The details on the synthesis of $CrNiSb_2$ were not given in the previous report,[30] and we could not reproduce $CrNiSb_2$ using the solid-state method with binary pnictides, or elements as precursors neither at ambient, nor at high pressure (up to 8 GPa). Efforts of preparing related $CuMSb_2$ (M = Cr, Mn, Fe, Co), $CuNiAs_2$, and $AgNiSb_2$ with similar procedures at ambient pressure only yielded binary pnictides.
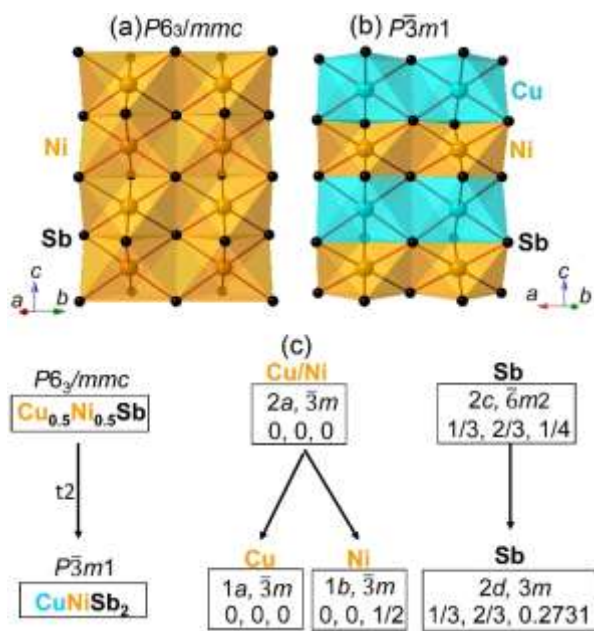

Figure 1. Structure of theoretical metal disordered $Cu_{0.5}Ni_{0.5}Sb$ with NiAs-type structure (a, $P6_3/mmc$), $CuNiSb_2$ with metal-ordered NiAs-derived structure (b, $P\overline{3}m1$ space group), and the group-subgroup relations between those two space groups (c).

Laboratory PXD and SPXD data analysis indicates that $CuNiSb_2$ crystallizes in the $P\overline{3}m1$ space group, in agreement with previous reports on the mineral samples. The calculated PXD pattern of $CuNiSb_2$ with $P\overline{3}m1$ space group is very similar to that of the calculated disordered $Cu_{0.5}Ni_{0.5}Sb$ with NiAs-type structure in $P6_3/mmc$ space group (Figure 2). Compared to the $P\overline{3}m1$ space group, there are fewer reflections in the $P6_3/mmc$ space group due to higher symmetry group with the following reflection conditions: $00l$: $l = 2n$; hkl: $l = 2n$, or $h - k + l = 3n +1$ or $3n +2$. As a result, (001), (003), (111), and (113) reflections are absent in the $P6_3/mmc$ space group but are allowed in the $P\overline{3}m1$ space group. Those reflections are also observed in the experimental PXD pattern, therefore, the published structure of mineral $CuNiSb_2$ with $P\overline{3}m1$ space group was used as the starting model for the Rietveld refinements (Figure 3). In this model, Cu and Ni atoms occupy the $1a$ (0, 0, 0) and $1b$ (0, 0, ½) positions,

respectively. We also tried another model with antisite disorder between Cu and Ni on both sites, but there was no improvement of the fitting, and the results contradicted with EDX results. If we constrained 50/50% of disordered Cu/Ni on both sites, the refinement resulted in two very different Cu/Ni-Sb bond distances (2.723 Å and 2.616 Å), which is not reasonable. Therefore, we performed the refinement with ordered Cu and Ni atoms in the $P\bar{3}m1$ space group (Figure 3).
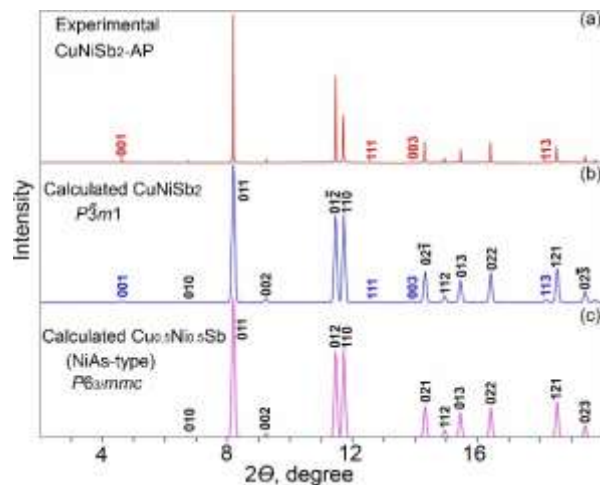

Figure 2. PXD patterns of experimental (a) and calculated (b) $CuNiSb_2$ with $P\bar{3}m1$ space group (b), and calculated $Cu_{0.5}Ni_{0.5}Sb$ with $P6_3/mmc$ space group (c).
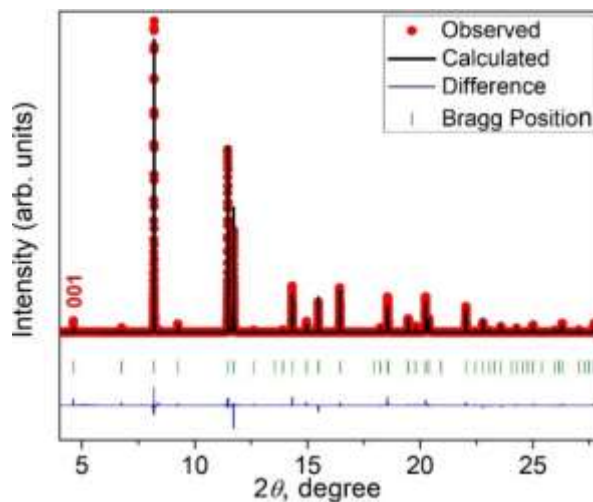
Figure 3. Rietveld refinement of SPXD of $CuNiSb_2$-AP in the $P\bar{3}m1$ space group with observed data (red), calculated pattern (black), Bragg position (green), and the difference between the observed and calculated pattern (blue).

In the refined structure, Sb atoms are arranged in a dense hexagonal packing with Cu and Ni occupying the octahedral sites (Figure 1). Each $CuSb_6$ or $NiSb_6$ octahedron connects with six octahedra by edge-sharing in the hexagonal ab plane. Alternate layers of $CuSb_6$ and $NiSb_6$ stack via face sharing along the crystallographic c axis and form the layered structure. The structure can be viewed as metal ordered NiAs-type ($P6_3/mmc$) derivative because $P\bar{3}m1$ (#164) space group is one of the subgroups of $P6_3/mmc$ (#194) based on Bärnighausen tree formalism, as shown in Figure 1c.[51] In the NiAs structure, Ni and As atoms occupy the special Wyckoff site 2a (0, 0, 0) and 2c (1/3, 2/3, 1/4), respectively. The

two-fold 2a Ni site in the $P6_3/mmc$ space group splits into the one-fold 1a (0, 0, 0) and 1b (0, 0, ½) sites to accommodate the ordering of Cu and Ni atoms in the $P\bar{3}m1$ space group. Because of the unequal size of CuSb$_6$ and NiSb$_6$ octahedra, the symmetric Sb hexagonal dense packing is distorted. Sb atoms are closer to smaller Ni atoms and form smaller NiSb$_6$ layers. As a result, position 2c (1/3, 2/3, 1/4) in the $P6_3/mmc$ shifts to position 2d (1/3, 2/3, 0.2731) in the lower-symmetry $P\bar{3}m1$ space group.

The refined parameters and structure information are given in Tables 1-2. The occupancy of each site has been refined, but there are no obvious vacancies. The refined lattice parameters using SPXD data are $a = b = 4.05685(1)$ Å, c = 5.13363(1) Å, V = 73.1701(2) Å^3, which are close to the reported values (a = b = 4.0510(2) Å, c = 5.1382(4) Å, V = 73.02 (1) Å^3).[26] The refined Cu, Ni, Sb atoms occupy the 1a (0, 0, 0), 1b (0, 0, ½), and 2d (0, 0, 0.2731), respectively. Cu-Sb, Ni-Sb bond distances are refined to be 2.7299(2) Å and 2.6159(1) Å, respectively (Table 2). The bond distances are very close to the sum of covalent radii of Cu (1.32 Å), Ni (1.24 Å), and Sb (1.39 Å),[28] which indicates the covalent nature of bonding between Cu/Ni and Sb atoms. The smaller Ni-Sb than Cu-Sb bond distance implies that the electron localization environment of Ni-Sb and Cu-Sb are different, which will be further discussed in the electronic structure section. The Ni-Sb bond distance (2.6159 Å) is close to the reported value (2.6174Å) of binary NiSb ($P6_3/mmc$),[52,53,54,55] but smaller than those (2.6750 Å, 2.7303 Å) in the disordered MnNiSb$_2$ and CrNiSb$_2$ ($P6_3/mmc$).[30, 31] The Cu-Ni transition metal bond distances are 2.5668(1) Å, which is close to the Ni-Ni (2.575 Å) metal bonds observed in NiSb, but smaller than those in MnNiSb$_2$ (2.700 Å) and CrNiSb$_2$ (2.660 Å).

Table 1. Selected Refined Structure Parameters of Polycrystalline and Single Crystal of CuNiSb$_2$ Samples

Sample	CuNiSb$_2$-AP				CuNiSb$_2$-8GPa				CuNiSb$_2$-Single Crystal		
Empirical formula	CuNiSb$_2$				CuNiSb$_2$				Cu$_{0.95(4)}$Ni$_{0.95(4)}$Sb$_2$		
Temperature	300 K				300 K				150 K		
Mol. Wt.	365.76				365.76				359.64		
X-ray wavelength, λ	0.414532 Å				0.412718 Å				0.71073 Å		
Space group, #	$P\bar{3}m1$, #164				$P\bar{3}m1$, #164				$P\bar{3}m1$, #164		
Z	1				1				1		
Lattice parameters	a = b= 4.05685(1) Å, c = 5.13363(1) Å, V = 73.1701(2) Å^3 $\alpha = \beta = 90°$, $\gamma = 120°$				a = b= 4.05692(1) Å, c = 5.12467(1) Å, V = 73.0446(1) Å^3 $\alpha = \beta = 90°$, $\gamma = 120°$				a = b= 3.9692(1) Å, c = 5.1297 (1) Å, V = 69.989(2) Å^3 $\alpha = \beta = 90°$, $\gamma = 120°$		
R indices	R_{exp} = 9.04%, R_F = 6.73%, R_{Bragg} = 8.38%				R_{exp} = 5.58%, R_F = 8.52%, R_{Bragg} = 8.25%				R_1 = 2.18%, wR_2 = 4.72%		
Site	Wyckoff symbol	x, y, z	Occ.		Site	x, y, z	Occ.		Site	x, y, z	Occ.
Cu	1a	0, 0, 0	1		Cu/Ni	0, 0, 0	0.5/0.5		Cu/Ni	0, 0, 0	0.5/0.5
Ni	1b	0, 0, 0.5	1		Cu/Ni	0, 0, 0.5	0.5/0.5		Cu/Ni	0, 0, 0.5	0.5/0.5
Sb	2d	1/3, 2/3, 0.2731(1)	1		Sb	1/3, 2/3, 0.2426(1)	1		Sb	1/3, 2/3, 0.2530(1)	1

Table 2. Selected Bond Distances in CuNiSb$_2$ and Related Compounds.

Comp.	Space group	Ni-Sb, Å	Cu-Sb, Å	M[a]-M, Å	Sb-Sb, Å
CuNiSb$_2$-AP	$P\bar{3}m1$	2.6159 (1)	2.7299(2)	2.5668 (1)	3.3031(3), 3.6536(3)
CuNiSb$_2$-8GPa	$P\bar{3}m1$	2.6519(3), 2.6882(3)		2.5623(2)	3.4159(6), 3.5277(7)
CuNiSb$_2$-Single Crystal	$P\bar{3}m1$	2.6185 (2), 2.6337 (2)		2.5649(2)	3.4163(4), 3.4628(4)
MnNiSb$_2$[31]	$P6_3/mmc$	2.6750	-	2.700	3.5530
CrNiSb$_2$[30]	$P6_3/mmc$	2.7303	-	2.660	3.5724
MnCrSb$_2$[56]	$P6_3/mmc$	-	-	2.8505	3.7104
NiSb[52]	$P6_3/mmc$	2.6174	-	2.5750	3.4386
Sb[57]	$P6_3/mmc$	-	-	-	3.2456 3.330

[a]M = Cu,Mn,Cr,Ni
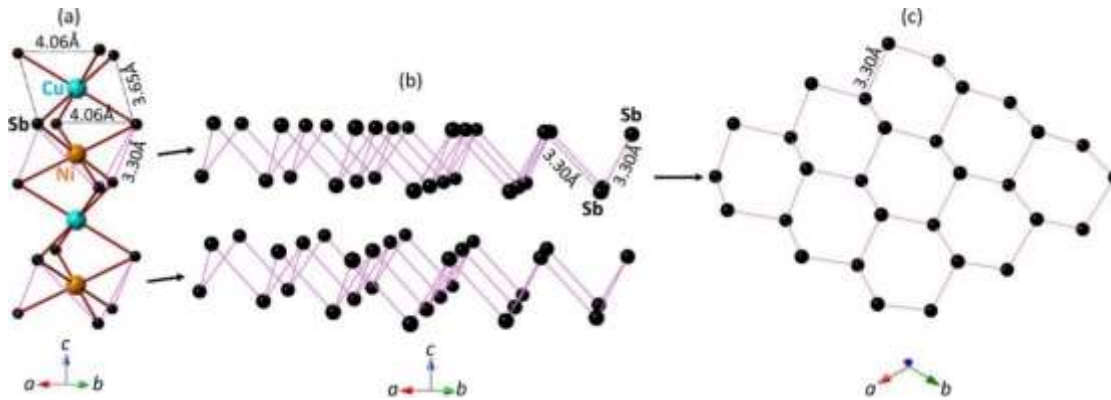
Figure 4. (a) Crystal structure with Sb-Sb distances, (b) layers of Sb-Sb connection within NiSb$_6$ layers, (c) perspective view of Sb-Sb connection in one layer along the c axis.

The shortest interlayer Sb-Sb lengths in NiSb$_6$ and CuSb$_6$ layers are 3.3031(3) Å and 3.6536(3) Å, respectively (Table 2, Figure 4a). The intralayer Sb-Sb distances are 4.0569 Å. The Sb-Sb distances are comparable with those in NiSb, but shorter than that of MnNiSb$_2$, CrNiSb$_2$, MnCrSb$_2$ (Table 2). The Sb-Sb distance (3.3031 Å) is much longer than the normal range of single Sb-Sb bond (~2.8 Å),[58] but close to those of hexagonal elemental Sb (3.2456 Å, 3.330 Å).[57] The long Sb-Sb distances can be considered as a weak hypervalent bond that has been observed in some other Sb-containing intermetallic compounds,[58] such as, Li$_2$Sb (Sb-Sb = 3.26 Å),[59] BaZnSb$_2$ (Sb-Sb = 3.24 Å)[60] Ca$_{14}$MnSb$_{11}$/Eu$_{14}$MnSb$_{11}$ (Sb-Sb = 3.22-3.26 Å),[61,62] and Ba$_7$Ga$_4$Sb$_9$ and Ba$_7$Al$_4$Sb$_9$ (Sb-Sb = 3.3 Å).[63,64] The Sb-Sb long weak bonds are arranged in a zig-zag array within the NiSb$_6$ layers (Fig.4b), and Sb and Sb are connected as a distorted hexagonal net along the crystallographic *ab* plane (Fig. 4c). If we consider the elongated Sb-Sb distance as a half bond (one-electron per bond) as suggested by Jeitschko and Mar,[65,66] each Sb has 5 lone electrons to meet the octet rule; then the formal charge on each Sb in the hexagonal net is -1.5. If we assume the formal charge of Cu and Ni are +1, +2, respectively, CuNiSb$_2$ can be ideally written as $Cu^{1+}Ni^{2+}(Sb^{1.5-})_2$ or $Cu^{1+}Ni^{2+}(Sb_2)^{3-}$. The real interactions between atoms in intermetallic compounds are complicated, and more discussions are included in the electronic

structure section. Based on the observed bond distances, the three-dimensional layered framework of CuNiSb$_2$ is mainly constructed by Ni-Sb, Cu-Sb, and Cu-Ni bonds.

CuNiSb$_2$ is a rare example of ternary '112' transition metal pnictide with metal-ordered NiAs-derived structure, considering that MnNiSb$_2$, MnCrSb$_2$, and CrNiSb$_2$ all adopt the NiAs-type ($P6_3/mmc$) structure with disordered metals.[28,30,31] The covalent radii difference (0.15 Å) between Cr ($r = 1.39$ Å)/Mn ($r = 1.39$ Å) and Ni ($r = 1.24$ Å) is larger than that (0.08 Å) between Cu ($r = 1.32$ Å) and Ni ($r = 1.24$ Å).[28] The different Cu-Sb and Ni-Sb covalent bonding strength may be responsible for stabilizing the metal ordering of the CuNiSb$_2$ structure. The total energy of stabilizing the metal-ordered NiAs-derived structure is lower than that of the NiAs-type ($P6_3/mmc$) structure, as discussed later in the electronic structure section. The recent report of HfMnSb$_2$ is another example of '112' pnictides with metal-ordering,[25] which is attributed to the large size difference between Hf ($r = 1.75$ Å) and Mn ($r = 1.39$ Å) atoms, similar to the scenario observed in AuNiSn$_2$ and AuCuSn$_2$.[23]

The average size of obtained polycrystalline particles is less than 100 μm, based on the SEM-EDX results (Figure S2). EDX mapping and microanalysis of 1 mm ×1mm area of particles indicated the homogeneous distribution of Cu, Ni, and Sb elements (Figure 5). The molar ratio of Cu: Ni: Sb is close to 1: 1: 2, which is good agreement with the Rietveld refinement results.
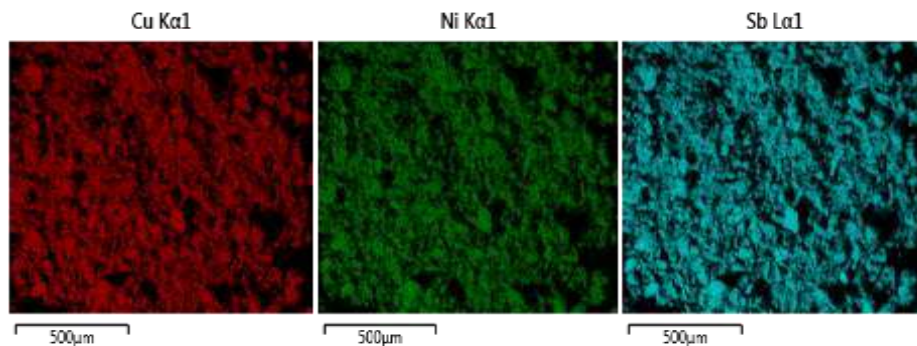
Figure 5. Energy-dispersive X-ray (EDX) elemental mapping of CuNiSb$_2$-AP particles.

The stability of the CuNiSb$_2$-AP phase was studied via thermogravimetric analysis (TGA) and differential scanning calorimetry (DSC) technique (Figure 6). Powder samples (~ 25 mg) were heated in an alumina crucible from 25 °C to 1200 °C and held at this temperature for 1 hour, and then cooled down to 100 °C at a rate of 10 °C/min. The sample is stable below 800 °C, based on the relatively stable mass. However, the sample mass starts decreasing above 800 °C, remains about 90% of its initial mass as the temperature reaches 1200 °C, and drops to 70% after 1 hour. After the TGA, the remaining sample was a shinning ball, which was mainly a mixture of NiSb, Cu$_2$Sb, Cu$_3$Sb, and Sb according to the PXD results (Figure S3). The decreased mass is due to the loss of Sb that with low melting point (630.6 °C) and high vapor pressure, a resulted component from the decomposition happening at high temperature. Two obvious endothermal peaks were observed in the DSC curve during cooling at 867 °C and 910 °C, which is probably related to the re-crystallization of the binary pnictides (Figure 6). A small exothermal peak at 591 °C observed during the heating process may be an indication of the cation order to disorder process in the structure, which requires in-situ synchrotron or neutron diffraction for confirmation in the future study.
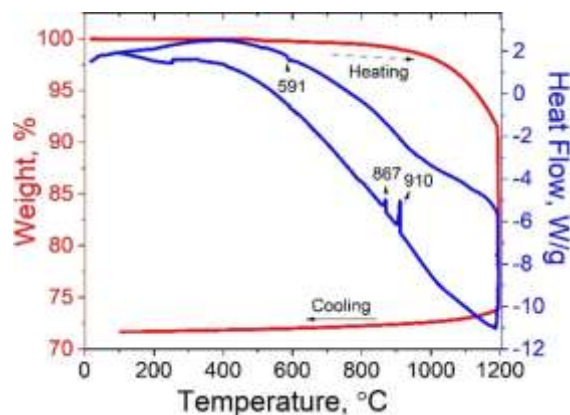
Figure 6. TGA-DSC data of CuNiSb$_2$-AP measured between 25 °C and 1200 °C.

Structure at High Pressure. Among all the reported 3d transition metals '112'pnicitdes, CuNiSb$_2$ is the only example that shows metal ordering, while MnNiSb$_2$, MnCrSb$_2$, and CrNiSb$_2$ adopt the NiAs-type structure with disordered metals. [28,30,31] Considering that MnNiSb$_2$ was prepared at high pressure, we carried out the high pressure experiment to investigate the possible structural transition. The CuNiSb$_2$-AP powders were assembled into a Walker-type multi-anvil high pressure press. After applying the pressures (8 GPa), the sample was heated at 700 °C for 1 h before quenching quickly to room temperature. The resulting pellet (sample CuNiSb$_2$-8GPa) was ground and checked by PXD. In comparison to the PXD pattern of CuNiSb$_2$-AP, the intensity of (001) reflection seems to decrease as the pressure increases from 6 to 8 GPa. As discussed above, the absence of (001) reflection is a signature of the formation of possible metal-disordered NiAs-type structure. However, the (001) reflection is weak in the PXD pattern of CuNiSb$_2$-AP sample, and the intensity of this easy-axis reflection may be reduced due to the strong preferred orientation under the high pressure.

To examine if the structure of CuNiSb$_2$-AP changes to NiAs-type structure under high pressure, electron diffraction patterns were taken (Figure 7). For electron diffraction patterns, conclusions cannot be based on the presence of the (001) or (010) reflections, as these could be caused by double diffraction. However, the presence of the $hhl:l=odd$ reflections on the [$\bar{1}$10] electron diffraction patterns agrees with $P\bar{3}m1$ but not with $P6_3/mmc$, and their presence cannot be explained through double diffraction paths. The results were consistent for all particles for which this particular zone could be obtained (8 for CuNiSb$_2$-AP and 4 for CuNiSb$_2$-8GPa). These results clearly indicate that NiAs-type ($P6_3/mmc$) structure under 8 GPa does not form. Rietveld refinement of SXRD data of CuNiSb$_2$-8GPa sample was carried out with $P\bar{3}m1$ space group and March-Dollase Multiaxial Function preferred orientation function including (001) and (101) reflections, which yielded the refined unit cell parameters: $a = b = 4.05692(1)$ Å, $c = 5.12467(1)$ Å, V = 73.0446(1) Å^3. The a parameter increases slightly, and the c parameter and volume decreases compared to those ($a = b = 4.05685$ Å, c = 5.13363 Å, V = 73.1701 Å^3) of CuNiSb$_2$-AP (Table 1). The overall structure is compressed slightly at 8 GPa. The initial model is the same used for CuNiSb$_2$-AP with Cu and Ni occupying the (0, 0, 0), and (0, 0, ½), respectively. However, the Sb position shifts to (0, 0, 0.2461), in comparison to that (0, 0, 0.2731) of CuNiSb$_2$-AP sample, which causes the Cu-Sb and Ni-Sb bond distances to become 2.6519 (3) Å and 2.6882 (Å) in CuNiSb$_2$-8GPa. The Sb position is close to the (0, 0, 0.25) and the almost equal M-Sb (M = Cu, Ni) bond distances indicate that a model with disordered Cu/Ni on both (0, 0, 0), and (0, 0, ½)

10

sites is more reasonable. Due to the close electron density between Cu and Ni, however, a reliable percentage of Cu/Ni on each site cannot be determined with X-ray technique or electron diffraction. Therefore, the structure was finalized with totally disordered Cu/Ni on both sites, as shown in Table 1 and Figure 8. The Sb position shift mainly causes one Sb-Sb bond distance increase, and the other one decreases, as shown in Table 2. However, the Cu-Ni distance is only related to the unit cell parameter c and therefore decreases as expected when unit parameter c decreases under 8 GPa. The CuNiSb$_2$-8GPa sample was obtained at 700 °C for 1 h, the high temperature probably causes the Cu/Ni atoms to migrate between (0, 0, 0) and (0, 0, ½) sites around 591°C as indicated in the DSC plot (Figure 6), or both high pressure and high pressure cause the structural transition.
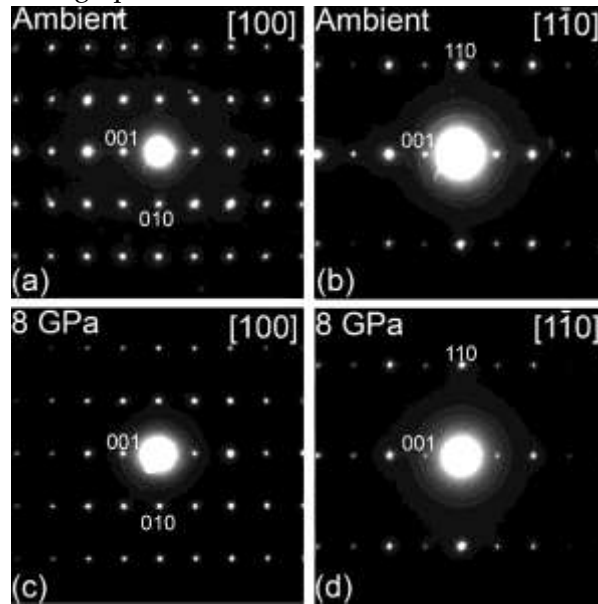
Figure 7. Representative electron diffraction patterns of CuNiSb$_2$-AP (a,b) and CuNiSb$_2$-8GPa (c, d).
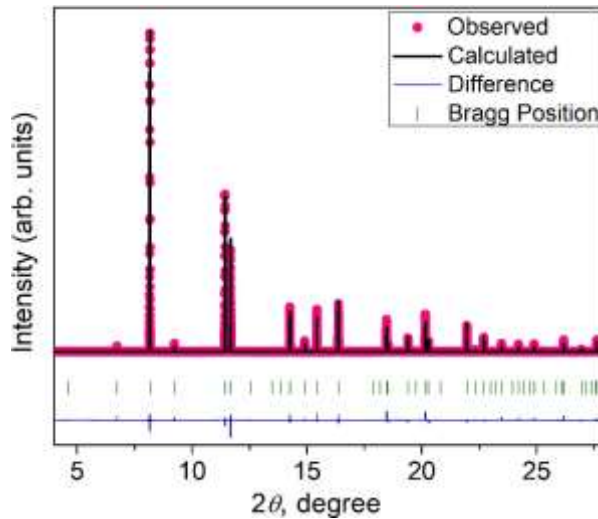
Figure 8. Rietveld refinement of SPXD of CuNiSb$_2$-8GPa in the $P\bar{3}m1$ space group with observed data (pink), calculated pattern (black), Bragg position (green), and the difference between the observed and calculated pattern (blue).

Single Crystal Structure. Single crystals were grown using CuNiSb$_2$-AP as starting material and AlCl$_3$ as transport reagent at 800-765 °C. A few small (< 0.1mm) crystals were obtained and selected for the single crystal X-ray diffraction measurement. The data collection was carried out at 150 K instead of 300 K, because of the low freezing point of the mineral oil used to support the single crystal. The trigonal crystal system is confirmed with the $P\bar{3}m1$ space group. Based on the electron density, transition metals occupy (0, 0, 0) and (0, 0, ½) sites, and Sb atoms occupy (0, 0, 0.2530) site. The position of Sb is nearly identical to that of CuNiSb$_2$-8GPa sample. Similarly to the refinement of CuNiSb$_2$-8GPa sample, the best single crystal refinement is obtained by assigning disordered Cu/Ni on both (0, 0, 0) and (0, 0, ½) sites, which in the single crystal case apparently also contain 5% vacancies. The refined structural information and related parameters are given in Table 1-2 and S1. The refined unit cell parameters ($a = b = 3.9692$ Å, $c = 5.1297$ Å, $V = 69.989$ Å^3) are significantly smaller than those of CuNiSb$_2$-AP ($a = b = 4.05685$ Å, $c = 5.13363$ Å, $V = 73.1701$ Å^3) and CuNiSb$_2$-8GPa ($a = b = 4.05692$ Å, $c = 5.12467$Å, $V = 73.0446$Å^3) samples. The crystal structure is relatively compressed within the *ab* plane at the low temperature. The refined Cu/Ni-Sb distances are 2.6185 (2) and 2.6337 (2) Å, and are smaller than those in both polycrystalline phases, due to the smaller *a* and *b* parameters. As shown in Table 2, the M-M (M = Cu, Ni) and Sb-Sb distances are comparable to that of CuNiSb$_2$-8GPa sample because of the similar *c* parameter and identical Sb positions. The cation disorder in the single crystal is consistent with the use of high temperatures during the crystal growth.

Physical Properties. Magnetic susceptibility as a function of temperature was conducted on CuNiSb$_2$-AP powder samples with an applied magnetic field of 1 T. The data is noisy due to the weak signal of magnetic susceptibility (~3×10^{-4} emu/mol at 2 K). The bump at 75 K is due to the transition from paramagnetic (< 75 K) to diamagnetic (> 75 K) region with raw data above 75 K being negative. The diamagnetic correction was approximately carried out by subtracting the reported Pascal constants of Cu$^+$ (-12 ×10^{-6} emu/mol), Ni^{2+} (-12 ×10^{-6} emu/mol), and covalent Sb (III , -74 ×10^{-6} emu/mol).[67] The overall trend shown in Figure 9 indicates that CuNiSb$_2$-AP is Pauli paramagnetic, which is similar to the magnetic behavior observed in NiSb.[68]
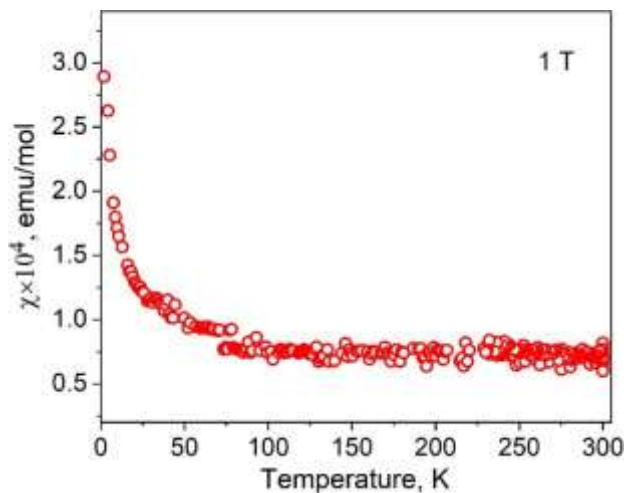

Figure 9. Temperature-dependent magnetic susceptibility of CuNiSb$_2$-AP with an applied magnetic field of 1T.

CuNiSb$_2$-AP powder samples were pressed into a dense pellet (91% density) to measure the thermoelectric properties because some related '112' materials such as CuTmTe$_2$ and AgTmTe$_2$ have shown good properties.[17,18] The PXD pattern of the dense pellet indicates the phase does not change after the SPS treatment (Figure S5). Resistivity (ρ) was measured from 2 to 300 K with the thermal transport option (TTO) two-point method with a PPMS. The alternating current (AC) four-point measurement transport option was not carried out. In low resistivity systems, it is known that using a two-probe method can overestimate resistivity by up to an order of magnitude due to contact resistance.[69] The resistivity increases as the temperature increases from 2 to 300 K, which indicates the sample is metallic (Figure 10), but the high residual resistivity at low temperature indicates this material falls in the range of bad metal. Fitting the data below 30 K with the function $\rho = \rho_0 + A\,T^n$ yields $\rho = 3.5 + 9.5T^3$, which indicates the electron-electron correlation and also some contributions from phonons. The n = 3 is between n = 2 for a good metal electron-electron correlations at low temperature, and n = 5 for phonon contributions.[70] Due to the metallic conductivity, the high thermal conductivity (~15 W/K·m at 300 K) (Figure 11) is expected. The Seebeck coefficient (~ 1 µV/K) is also very small (Figure S6), which renders this material a poor thermoelectric.
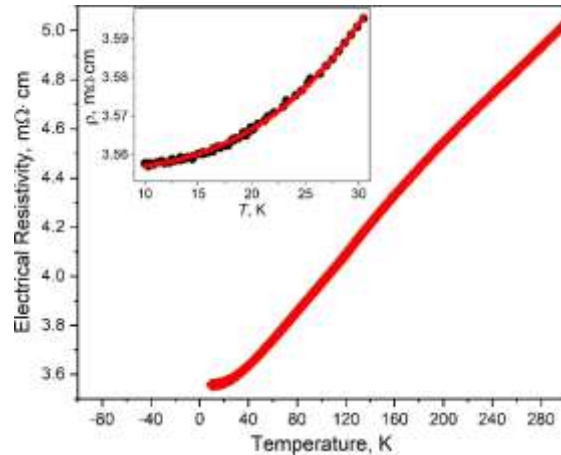

Figure 10. Electrical resistivity as a function of temperature. The inset shows the fitting with $\rho = \rho_0 + A\,T^n$ below 30 K.
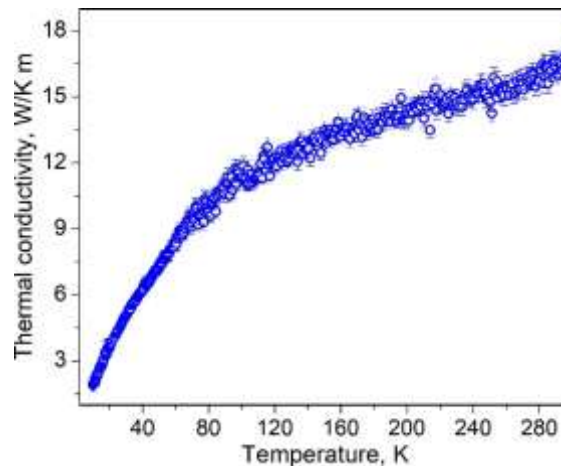

Figure 11. Thermal conductivity as a function of temperature.

Electronic Structures.

Unlike '112' chalcogenides such as $LiCrQ_2$ (Q = S, Se, Te), in which the formal oxidation states of cations and anions can be assigned as +1, +3, -2, respectively, based on the Zintl-Klemm concept that more electropositive elements are electron donors such as alkali, alkaline earth, and rare earth elements. The discussed formal charge above in $Cu^+Ni^{2+}Sb_2^{3-}$ cannot be simply interpreted using Zintl-Klemm concept due to 3d electrons. This interpretation is in contrast to the electronic structure, in which the valence band is mainly composed of transition metals Cu-d and Ni-d instead of Sb-p orbitals (Figure 12). The density of states (DOS) of CuNiSb$_2$-AP was calculated using both LMTO (Figure 12) and Wien2k (Figure S7) software that resulted in very similar results. The DOS of Cu, Ni, and Sb are distributed over the whole energy range from -6 eV to the Fermi level in the valence band, which suggests the strong hybridization between Cu/Ni and Sb with covalent bonding as the major bonding character.
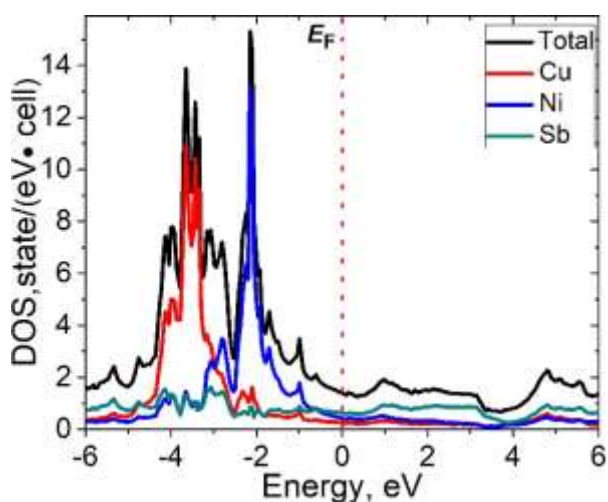
Figure 12. The density of state (DOS) of CuNiSb$_2$-AP.

The non-zero DOS at the Fermi level (E_F) indicates the metallicity of the compound, which is in agreement with the experimental resistivity measurement (Figure 10). The maximum DOS of Ni and Cu orbitals locates at lower energy (~ -2eV, -3.5 eV, respectively) below the E_F. The metallic nature and small DOS (small effective mass) at the E_F explain the small Seebeck coefficient observed in CuNiSb$_2$-AP. To understand that CuNiSb$_2$-AP adopts the metal-ordered NiAs-derived structure ($P\bar{3}m1$) instead of a metal-disordered NiAs-type structure ($P6_3/mmc$), we simulate the disordered NiAs structure with virtual crystal approximation (VCA). The calculations indicate that the energy of CuNiSb$_2$ in $P\bar{3}m1$ space group is much lower (19.9 eV/f.u.) than that in the $P6_3/mmc$ space group. We also carried out the CuNiSb$_2$-8GPa phase with metal-ordered NiAs-derived structure ($P\bar{3}m1$) using the unit cell parameters from the Rietveld refinement. The DOS is very similar to that of the CuNiSb$_2$-AP phase. Even though it is hard to precisely calculate the electronic structure of the CuNiSb$_2$-8GPa phase with the metal-disordered structure in the $P\bar{3}m1$ space group, the overall shape of DOS is probably the same.

To understand the bonding nature in CuNiSb$_2$, we carried out the crystal orbital Hamilton population (COHP) analysis of Ni-Sb, Cu-Sb, Cu-Ni, and Sb-Sb. The positive and negative –COHP represents bonding and antibonding, respectively. As shown in Figure 13, Ni-Sb and Cu-Sb bonding

14

states locate mainly below the E_F with weak bonding at the E_F. The nonbonding character of Ni-Sb is mainly at energy higher than the E_F up to 3 eV. The Ni-Sb and Cu-Sb covalent bonding are expected based on the bond distances observed, as discussed above, which is corroborated by the large negative integrated COHP (-ICHOP) of Ni-Sb (5.15 eV/bond) and Cu-Sb (3.16 eV/bond). The higher magnitude of -ICHOP of Ni-Sb is consistent with a stronger covalent bond in Ni- Sb than in Cu-Sb. The Cu-Ni bonding states are also observed at and near the E_F, with the overall –ICHOP of 1.49 eV/bond, which is smaller than those of Cu/Ni-Sb. The antibonding states of Sb-Sb exist at the E_F, but there are bonding characters in energy ranges of –6 eV to -4eV and –2 eV to -1 eV. The overall–ICHOP of 0.83 eV/bond suggests weak Sb-Sb interactions in the structure.
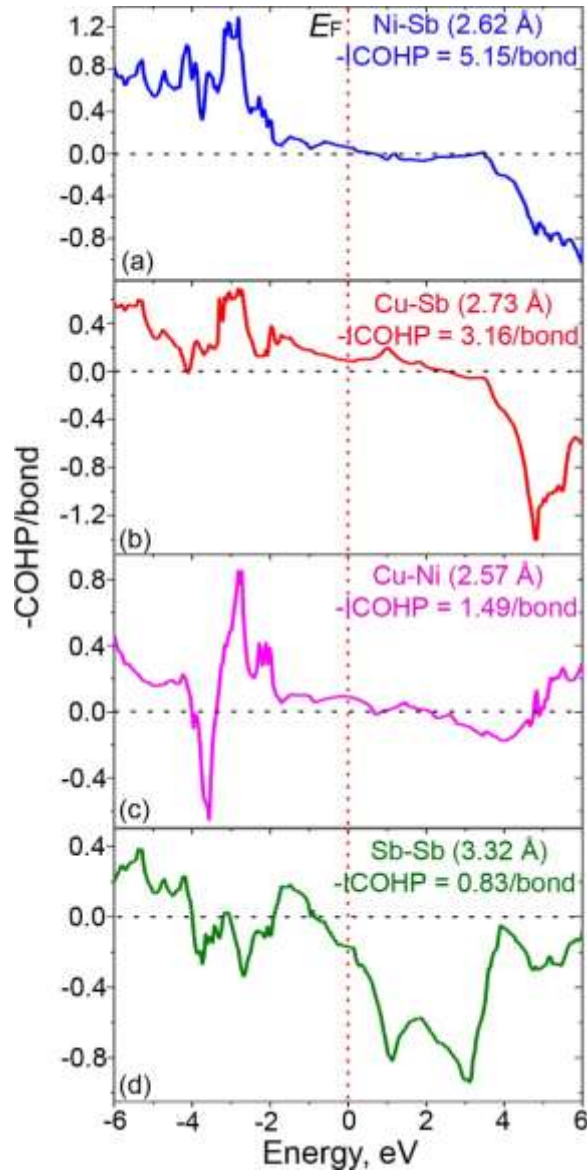
Figure 13. Crystal orbital Hamilton population (COHP) plots of Ni-Sb (a), Cu-Sb (b), Cu-Ni(c) , and Sb-Sb (d) interactions in CuNiSb$_2$-AP.

The bonding nature of CuNiSb$_2$ is further studied with electron localization function (ELF) and charge density distribution (Figure 14). A slice of ELF that included all Cu, Ni, and Sb atoms are shown in Figure 14b, with the corresponding charge density distribution displayed in Figure 14c. The highest electron localization is around Sb atoms, and there are electrons distributed between the nearest Sb atoms. The larger area of lowest electron localization around Ni than that of Cu indicates that Ni shared more electrons with Sb atoms for forming Cu/Ni-Sb bond. However, a maximum is not observed between Cu/Ni-Sb to directly confirm the covalent bond using ELF analysis. The charge density distribution clearly shows the highest charge around Ni atoms and its extension to neighboring Sb atoms, indicating strong Ni-Sb bonding. Cu-Sb and Cu-Ni bonding also exist based on the charge density distribution. The absence of the minimum of electron localization and charge density between Sb atoms indicates the existence of the weak Sb-Sb bonding. Both ELF and charge density distribution results support the COHP analysis with the bonding strength decreases in the order of Ni-Sb, Cu-Sb, Cu-Ni, and Sb-Sb bonding.
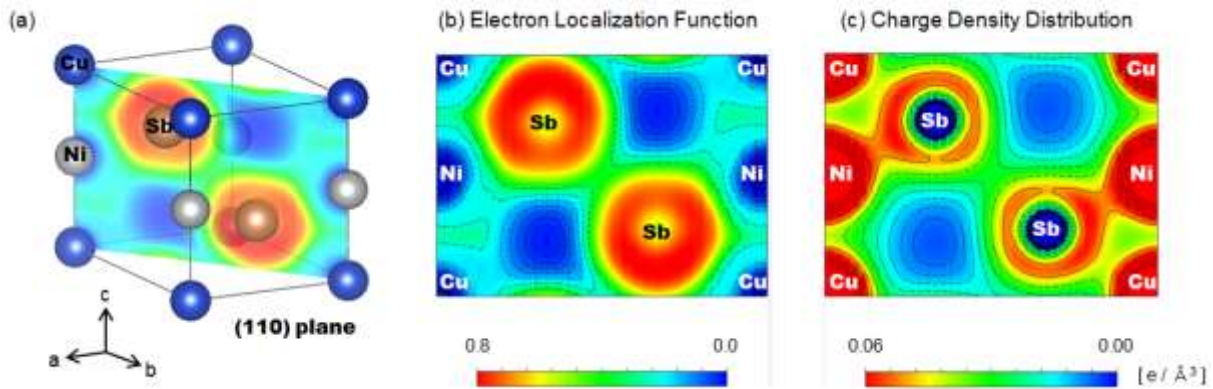

Figure 14. Structure of CuNiSb$_2$-AP with a (110) slice of ELF (a), electron localization function (b), and partical charge density distribution integrated from E_F – 2 eV to E_F (c) in the (110) plane.

CONCLUSION

Polycrystalline CuNiSb$_2$ was successfully synthesized at ambient pressure for the first time with a two-step solid-state method. Single crystals were also obtained by chemical vapor transport. Rietveld refinements based on synchrotron X-ray diffraction data indicate that CuNiSb$_2$ adopts a cation-ordered NiAs-derived structure type in $P\overline{3}m1$ space group instead of NiAs structure ($P6_3/mmc$), which is ascribed to the significantly lower energy of the ordered structure relative to the disordered one as confirmed by first principle calculations. The structure is constructed by Ni-Sb, Cu-Sb covalent bonds, Cu-Ni metallic bonds, and weak Sb-Sb interactions, which is supported by the bond lengths, calculations of COHP, ELF, and charge density. The space group symmetry remains unchanged when the sample is pressed at 8 GPa high pressure and 700 °C, but the cations appear to disorder, which is also observed in the single crystal structure refinement. The specific effect of high pressure on the structure is undergoing and will report the results in due course. Both the temperature dependence of resistivity and the calculated DOS indicate that CuNiSb$_2$ is metallic. The Pauli paramagnetism, low Seebeck coefficient, high thermal conductivity indicate that CuNiSb$_2$ is not a potential magnetic or

thermoelectric material. However, $CuNiSb_2$ represents a rare case of '112' in ternary pnictides and provides a reference for further study of '112' compounds, of which many are predicted to be promising thermoelectrics.[22] More '112' ternary pnictides such as $T_1T_2Pn_2$ or $RTPn_2$ (T = transition metal, R = rare-earth metal) with metal-ordered NiAs-derived structure require further exploration using solid-state methods at ambient and high pressure, and/or other synthetic methods including Sb, Bi, and salt fluxes.

ASSOCIATED CONTENT

Supporting Information. Refined structural parameters of single crystal; PXD patterns of samples after the first annealing step, TGA measurement, SPS treatment, and $CuNiSb_2$-8GPa; overall elemental mapping of $CuNiSb_2$-AP; Seebeck coefficient of $CuNiSb_2$-AP; DOS and band structure of $CuNiSb_2$-AP using the WIEN2k software.

Accession Codes. CCDC number 2010628 contains the supplementary crystallographic data for this paper. These data can be obtained free of charge from FIZ Karlsruhe via www.ccdc.cam.ac.uk/structures . or by emailing data_request@ccdc.cam.ac.uk, or by contacting The Cambridge Crystallographic Data Centre, 12 Union Road, Cambridge CB2 1EZ, UK; fax: +44 1223 336033.

AUTHOR INFORMATION

Corresponding Authors* E-mail: xtan6@gmu.edu, greenbla@chem.rutgers.edu.
Authors ORCID: Callista M. Skaggs: 0000-0002-4380-2201, Chang-Jong Kang: 0000-0003-2895-4888, Christopher J. Perez: 0000-0002-1088-0190, Corey E. Frank: 0000-0003-2638-7795, Gabriel Kotliar: 0000-0001-6366-7687, Susan M. Kauzlarich: 0000-0002-3627-237X, Xiaoyan Tan: 0000-0002-1742-8252, Martha Greenblatt: 0000-0002-1806-2766.

Present Address
#National High Magnetic Laboratory, Tallahassee, FL, 32310, United States

ACKNOWLEDGMENTS

REFERENCES

(1)   Villars. P. *Pearson's Handbook: Desk Edition: Crystallographic Data for Intermetallic Phases Rev Sub Edition*; ASM International: Materials Park, 1997.

(2)   White, J. G.; Pinch, H. L. The Crystal Structure of Lithium Thiochromite, $LiCrS_2$. *Inorg. Chem.* **1970**,

9, 2581–2583.

(3)   Laar, B. van; Ijdo, D. J. W. Preparation, Crystal Structure, and Magnetic Structure of LiCrS$_2$ and LiVS$_2$. *J. Solid State Chem.* **1971**, *3*, 590–595.

(4)   Kobayashi, S.; Ueda, H.; Michioka, C.; Yoshimura, K. Competition Between the Direct Exchange Interaction and Superexchange Interaction in Layered Compounds LiCrSe$_2$, LiCrTe$_2$, and NaCrTe$_2$ with a Triangular Lattice. *Inorg. Chem.* **2016**, *55*, 7407–7413.

(5)   Dahn, J. R.; McKinnon, W. R.; Haering, R. R.; Buyers, W. J. L.; Powell, B. M. Structure Determination of Li$_x$TiS$_2$ by Neutron Diffraction. *Can. J. Phys.* **1980**, *58*, 207–213.

(6)   Le Blanc, A.; Rouxel, J. Structural Types of Intercalation Compounds MSnS$_2$ (M = Li, Na, K, Rb). *C. R. Acad. Sci, Ser. C: Chem.* **1972**, *274*, 786–788.

(7)   Guseinov, G. D.; Ismailov, M. Z.; Guseinov, G. On the New Semiconducting Compound CdTlS$_2$. *Mater. Res. Bull.* **1967**, *2*, 765–772.

(8)   Guseinov, G. D.; Guseinov, G. G.; Ismailov, M. Z.; Godzhaev, E. M. Structure and Physical Properties of New Semiconductor Compounds CdTlS$_2$(Se$_2$, Te$_2$). *Inorg. Mater.* **1969**, *5*, 27–32.

(9)   Avilov, A. S.; Agaev, K. A.; Guseinov, G. G.; Imamov, R. M. Determination of Crystals Structures of Some Three-Component Semiconductors with the Overall Formula A. *Kristallografiya* **1969**, *14*, 443–446.

(10)   Boller, H.; Klepp, K. O.; Kirchmayr, K. On the Knowledge of Two Thallium-Tellurochromites [TlCrTe$_2$ and TlCr$_5$Te$_8$]. *Mater. Res. Bull.* **1995**, *30*, 365–371.

(11)   Ronneteg, S.; Lumey, M. W.; Dronskowski, R.; Berger, R. The Magnetic Structure of TlCrTe$_2$. *J. Alloys Compd.* **2005**, *403*, 71–75.

(12)   Daszkiewicz, M.; Gulay, L. D.; Shemet, V. Y.; Pietraszko, A. Comparative Investigation of the Crystal Structure of LnCuSe$_2$ Compounds (Ln = Tb, Dy, Ho, Er, Tm, Yb, and Lu). *Z. Anorg. Allg. Chem.* **2008**, *634*, 1201–1204.

(13)   Gulay, L. D.; Daszkiewicz, M.; Shemet, V. Y. Crystal Structure of ∼RCu$_3$S$_3$ and ∼RCuTe$_2$ (R = Gd-Lu) Compounds. *J. Solid State Chem.* **2012**, *186*, 142–148.

(14)   Gulay, L. D.; Stępień-Damm, J.; Daszkiewicz, M.; Pietraszko, A. Crystal Structure of the TmAgTe$_2$ Compound. *J. Alloys Compd.* **2007**, *431*, L1-L3.

(15)   Shemet, V. Y.; Gulay, L. D.; Olekseyuk, I. D. Crystal Structures of the ScAgSe$_2$ and Sc$_{1.02}$Cu$_{0.54}$Sn$_{1.1}$S$_4$ Compounds. *J. Alloys Compd.* **2006**, *426*, 186–189.

(16)   Geller, S.; Wernick, J. H. Ternary Semiconducting Compounds with Sodium Chloride-like Structure: AgSbSe$_2$, AgSbTe$_2$, AgBiS$_2$, AgBiSe$_2$. *Acta Crystallogr.* **1959**, *12*, 46–54.

(17)   Lin, H.; Chen, H.; Shen, J. N.; Chen, L.; Wu, L. M. Chemical Modification and Energetically Favorable Atomic Disorder of a Layered Thermoelectric Material TmCuTe$_2$ Leading to High Performance. *Chem. - A Eur. J.* **2014**, *20*, 15401–15408.

(18)   Zhu, H.; Hautier, G.; Aydemir, U.; Gibbs, Z. M.; Li, G.; Bajaj, S.; Pöhls, J. H.; Broberg, D.; Chen, W.; Jain, A.; et al. Computational and Experimental Investigation of TmAgTe$_2$ and XYZ$_2$ Compounds, a New Group of Thermoelectric Materials Identified by First-Principles High-Throughput Screening. *J. Mater. Chem. C* **2015**, *3*, 10554–10565.

(19)   Pan, L.; Bérardan, D.; Dragoe, N. High Thermoelectric Properties of N-Type AgBiSe$_2$. *J. Am. Chem. Soc.* **2013**, *135*, 4914–4917.

(20)   Zou, M.; Liu, Q.; Wu, C. F.; Wei, T. R.; Tan, Q.; Li, J. F.; Chen, F. Comparing the Role of Annealing on the Transport Properties of Polymorphous AgBiSe$_2$ and Monophase AgSbSe$_2$. *RSC Adv.* **2018**, *8*, 7055–7061.

(21)   Li, S.; Feng, Z.; Tang, Z.; Zhang, F.; Cao, F.; Liu, X.; Singh, D. J.; Mao, J.; Ren, Z.; Zhang, Q. Defect Engineering for Realizing p-Type AgBiSe$_2$ with a Promising Thermoelectric Performance. *Chem. Mater.* **2020**, *32*, 3528-3536.

(22) Pöhls, J-H.; Luo, Z.; Aydemir, U.; Sun, J-P.; Hao, S.; He, J.; Hill, I. G.; Hautier, G.; Jain, A.; Zeng, X.; Wolverton, C.; Snyder, G. J.; Zhu, H.; White, M. A. First-Principles Calculations and Experimental Studies of XYZ$_2$ Thermoelectric Compounds: Detailed Analysis of van Der Waals Interactions. *J. Mater. Chem. A* **2018**, *6*, 19502–19519.

(23) Lange, S.; Nilges, T.; Hoffmann, R. D.; Pöttgen, R. The Stannides AuNiSn$_2$ and AuCuSn$_2$ - Bulk Synthesis and Superstructure Determination. *Z. Anorg. Allg. Chem.* **2006**, *632*, 1163–1166.

(24) Lange, S.; Schappacher, F. M.; Johrendt, D.; Nilges, T.; Hoffmann, R. D.; Pöttgen, R. 119Sn Mössbauer Spectroscopy and Chemical Bonding in AuTSn$_2$ (T = Ni, Cu, Pd). *Z. Anorg. Allg. Chem.* **2006**, *632*, 1432–1436.

(25) Murakami T.; Yamamoto, T.; Tassel, C.; Takatsu, H, Ritter, C.; Ajiro, Y.; Kageyama, H. HfMnSb$_2$: A Metal-Ordered NiAs-type Pnictide with a Conical Spin Order. *Angew. Chem. Int. Ed.* **2016**, *55*, 9877–9880.

(26) Rozenberg, K. A.; Rastsvetaeva, R. K.; Chukanov, N. V.; Pekov, I. V. Crystal Structure of a New Mineral CuNiSb$_2$. *Dokl. Phys.* **1994**, *39*, 224–226.

(27) Kabalov, Y.; Sokolova, E. Discovery of New Minerals Zlatogorite, Turkestanite and Belovite-(La) by Rietveld Refinement from X-Ray Powder Diffraction Data. *Mater. Sci. Forum* **1998**, *278–281*, 785–790.

(28) Cordero, B.; Gómez, V.; Platero-Prats, A. E.; Revés, M.; Echeverría, J.; Cremades, E.; Barragán, F.; Alvarez, S. Covalent Radii Revisited. *Dalt. Trans.* **2008**, *21*, 2832–2838.

(29) Reimersto, W.; Hellnerf, E.; Treutmann, W.; Hegerfo, G. Magnetic Phase Diagram of the System Mn$_{1-x}$Cr$_x$Sb (0≤x≤1). *J. Phys. C: Solid State Phys.* **1982**, *15*, 3597–3615.

(30) Varich, N.I.; Varich, A.N.; Kravtsov, I. A. Continuous Series of Solid Solutions between Intermetallic Compounds in Quasi-Binary Systems. *Reports Aca. Sci. Uka. SSR. Ser. A.* **1973**, *1*, 84–88.

(31) Kengo Adachi, Ryo Imura, Masaaki Matsui, and H. S. Spin Glass State of MnxNi1-XSb: Synthesis in High Pressure and High Temperature Atmospheres. *J. Phys. Soc. Japan* **1978**, *44*, 114–121.

(32) Chen, R. Y.; Zhang, S. J.; Zhang, M. Y.; Dong, T.; Wang, N. L. Revealing Extremely Low Energy Amplitude Modes in the Charge-Density-Wave Compound LaAgSb$_2$. *Phys. Rev. Lett.* **2017**, *118*, 107402.

(33) Kuo, C. N.; Shen, D.; Li, B. S.; Quyen, N. N.; Tzeng, W. Y.; Luo, C. W.; Wang, L. M.; Kuo, Y. K.; Lue, C. S. Characterization of the Charge Density Wave Transition and Observation of the Amplitude Mode in LaAuSb$_2$. *Phys. Rev. B* **2019**, *99*, 235121.

(34) Wang, K.; Petrovic, C. Large Linear Magnetoresistance and Magnetothermopower in Layered SrZnSb$_2$. *Appl. Phys. Lett.* **2012**, *101*, 152102.

(35) Liu, J.; Hu, J.; Cao, H.; Zhu, Y.; Chuang, A.; Graf, D.; Adams, D. J.; Radmanesh, S. M. A.; Spinu, L.; Chiorescu, I.; et al. Nearly Massless Dirac Fermions Hosted by Sb Square Net in BaMnSb$_2$. *Sci. Rep.* **2016**, *6*, 1–9.

(36) Walker, D.; Li, J. Castable Solid Pressure Media for Multianvil Devices. *Matter Radiat. Extrem.* **2020**, *5*, 018402.

(37) SMART and SAINT. Bruker AXS INc.: Madison, WI 2007.

(38) Sheldrick, G. M. A Short History of SHELX. *Acta Crysta.* **2008**, *64A*, 112–122.

(39) Bellaiche, L.; Vanderbilt, D. Virtual Crystal Approximation Revisited: Application to Dielectric and Piezoelectric Properties of Perovskites. *Phys. Rev. B: Condens. Matter Mater. Phys.* **2000**, *61*, 7877–7882.

(40) Giannozzi, P.; Baroni, S.; Bonini, N.; Calandra, M.; Car, R.; Cavazzoni, C.; Ceresoli, D.; Chiarotti, G. L.; Cococcioni, M.; Dabo, I.; Corso, A. D.; Gironcoli, S. d.; Fabris, S.; Fratesi, G.; Gebauer, R.; Gerstmann, U.; Gougoussis, C.; Kokalj, A.; Lazzeri, M.; Martin-Samos, L.; Marzari, N.; Mauri, F.; Mazzarello, R.; Paolini, St.; Pasquarello, A.; Paulatto, L.; Sbraccia, C.; Scandolo, S.; Sclauzero, G.; Seitsonen, A.P.; Smogunov, A.; Umari, P.; Wentzcovitch, R. M. QUANTUM ESPRESSO: A Modular and Open-Source Software Project for Quantum Simulations of Materials. *J. Phys.: Condens. Matter*

2009, *21*, 395502.

(41)   Giannozzi, P.; Andreussi, O.; Brumme, T.; Bunau, O.; Buongiorno Nardelli, M.; Calandra, M.; Car, R.; Cavazzoni, C.; Ceresoli, D.; Cococcioni, M.; Colonna, N.; Carnimeo, I.; Dal Corso, A.; de Gironcoli, S.; Delugas, P.; Di Stasio, R. A., Jr.; Ferretti, A.; Floris, A.; Fratesi, G.; Fugallo, G.; Gebauer, R.; Gerstmann, U.; Giustino, F.; Gorni, T.; Jia, J.; Kawamura, M.; Ko, H.-Y.; Kokalj, A.; Kucukbenli, E.; Lazzeri, M.; Marsili, M.; Marzari, N.; Mauri, F.; Nguyen, N. L.; Nguyen, H.-V.; Otero-de-la-Roza, A.; Paulatto, L.; Ponce, S.; Rocca, D.; Sabatini, R.; Santra, B.; Schlipf, M.; Seitsonen, A. P.; Smogunov, A.; Timrov, I.; Thonhauser, T.; Umari, P.; Vast, N.; Wu, X.; Baroni, S. Advanced Capabilities for Materials Modelling with Q Uantum ESPRESSO. *J. Phys. Condens. Matter* **2017**, *21*, 395502.

(42)   Hamann, D. R. Optimized Norm-Conserving Vanderbilt Pseudopotentials. *Phys. Rev. B: Condens. Matter Mater. Phys.* **2013**, *88*, 1–10.

(43)   Blöchl, P. E. Projector Augmented-Wave Method. *Phys. Rev. B* **1994**, *50*, 17953–17979.

(44)   Kresse, G.; Furthmüller, J. Efficiency of Ab-Initio Total Energy Calculations for Metals and Semiconductors Using a Plane-Wave Basis Set. *Comput. Mater. Sci.* **1996**, *6*, 15–50.

(45)   Kresse, G.; Furthmüller, J. Efficient Iterative Schemes for Ab Initio Total-Energy Calculations Using a Plane-Wave Basis Set. *Phys. Rev. B: Condens. Matter Mater. Phys.* **1996**, *54*, 11169–11186.

(46)   Joubert, D. From Ultrasoft Pseudopotentials to the Projector Augmented-Wave Method. *Phys. Rev. B: Condens. Matter Mater. Phys.* **1999**, *59*,1758–1775.

(47)   Perdew, J. P.; Burke, K.; Ernzerhof, M. Generalized Gradient Approximation Made Simple. *Phys. Rev. Lett.* **1996**, *77*, 3865–3868.

(48)   Blaha, P.; Schwarz, K.; Madsen, G. K. H.; Kvasnicka, D.; Luitz, J. *WIEN2K, An Augmented Plane Wave + Local Orbitals Program for Calculating Crystal Properties*. Technische Universität Wien: Wien: Austria, 2001.

(49)   Tank, R.; Jepsen, O.; Burkhardt, A.; Andersen, O. K. The Program TB-LMTO-ASA. Version 4.7; Max-Planck-Institut für Festkorperforschung: Stuttgart, 1999.

(50)   Fürtauer, S.; Flandorfer, H. A New Experimental Phase Diagram Investigation of Cu-Sb. *Monatsh. Chem.* **2012**, *143*, 1275–1287.

(51)   Baernighausen, H. Group-Subgroup Relations Between Space Groups: A Useful Tool in Crystal Chemist. *MATCH, Commun. Math. Chem.* **1980**, *9*, 139.

(52)   Zhuravlev, N. N.; Zhdanov, G. S.; Smirnova, Y. M. Investigation of Ternary Solid Solutions on the Basis of Superconducting Compounds. *Phys. Met. Metallogr.* **1962**, *13*, 55–61.

(53)   Kjekshus, A.; Walseth, K. P.; Rasmussen, S. E.; Heinegård, D.; Balaban, A. T.; Craig, J. C. On the Properties of the $Cr_{1+x}Sb$, $Fe_{1+x}Sb$, $Co_{1+x}Sb$, $Ni_{1+x}Sb$, $Pd_{1+x}Sb$, and $Pt_{1+x}Sb$ Phases. *Acta Chem. Scand.* **1969**, *23*, 2621–2630.

(54)   Makovetskii, G. I.; Shakhlevich, G. M. Phase Diagram and Certain Properties of Alloys of the NiSb - NiTe System. *Inorg. Mater.* **1982**, *18*, 186–189.

(55)   Lomnytska, Y. F.; Berezovets, V. V. Phase Relations in the Nb–Ni–Sb System. **2005**, *41*, 1324–1329.

(56)   Grazhdankina, N. P.; Medvedeva, I. V. Effect of High Pressure on Magnetic Properties of Manganese-Chromium-Antimony ($Mn_{1-x}Cr_xSb$) Alloys. *Fiz. Met. Metalloved.* **1983**, *55*, 96–101.

(57)   Dilshad, K.; Vankar, V. D.; Goel, T. C.; Chopra, K. L. Metastable Structures of Splat-Cooled and Vapor-Deposited Lead and Antimony Films. *Thin Solid Films* **1979**, *58*, 327–332.

(58)   Papoian, G. A.; Hoffmann, R. Hypervalent Bonding in One, Two, and Three Dimensions: Extending the Zintl-Klemm Concept to Nonclassical Electron-Rich Networks. *Angew. Chem. Int. Ed.* **2000**, *39*, 2408–2448.

(59)   Mueller, W. Preparation and Crystal Structure of Lithium Antimonide (Li_2Sb). *Z. Naturforsch. B: Anorg. Chem., Org. Chem., Biochem., Biophy. Bio.* **1977**, *32B*, 357–359.

(60)   Brechtel, Erwin; Cordier, Gerhard; Schaefer, H. New Ternary Alkaline Earth-Transition Element

Pnictide. *J. Less-Common Met.* **1981**, *79*, 131–138.

(61) Rehr, Anette; Kauzlarich, S. M. $Eu_{14}MnSb_{11}$, a Novel Rare Earth Metal Zintl Compound. *J. Alloys Compd.* **1994**, *207–208*, 424–426.

(62) Hu, Y.; Wang, J.; Kawamura, A.; Kovnir, K.; Kauzlarich, S. M. $Yb_{14}MgSb_{11}$ and $Ca_{14}MgSb_{11}$-New Mg-Containing Zintl Compounds and Their Structures, Bonding, and Thermoelectric Properties. *Chem. Mater.* **2015**, *27*, 343–351.

(63) Alemany, P.; Alvarez, S.; Hoffmann, R. The Electronic Structure of $Ba_7Ga_4Sb_9$, a Compound Seemingly Probing the Limits of the Zintl Concept. *Inorg. Chem.* **1990**, *29*, 3070–3073.

(64) He, H.; Stoyko, S.; Bobev, S. New Insights into the Application of the Valence Rules in Zintl Phases-Crystal and Electronic Structures of $Ba_7Ga_4P_9$, $Ba_7Ga_4As_9$, $Ba_7Al_4Sb_9$, $Ba_6CaAl_4Sb_9$, and $Ba_6CaGa_4Sb_9$. *J. Solid State Chem.* **2016**, *236*, 116–122.

(65) Brylak, M.; Möller, M. H.; Wolfgang, J. Ternary Arsenides $ACuAs_2$ and Ternary Antimonides $AAgSb_2$ (A = Rare-Earth Elements and Uranium) with $HfCuSi_2$-Type Structure. *J. Solid State Chem.* **1995**, *115*, 305–308.

(66) Ferguson, M. J.; Hushagen, R. W.; Mar, A. Crystal Structures of La_3ZrSb_5, La_3HfSb_5, and $LaCrSb_3$. Structural Relationships in Ternary Rare-Earth Antimonides. *J. Alloys Compd.* **1997**, *249*, 191–198.

(67) Bain, G. A.; Berry, J. F. Diamagnetic Corrections and Pascal's Constants. *J. Chem. Educ.* **2008**, *85*, 532–536.

(68) Kobayashi, H.; Kageshima, M.; Kimura, N.; Aoki, H.; Oohigashi, M.; Motizuki, K.; Kamimura, T. Magnetism and de Haas-Van Alphen Effect in NiSb. *J. Magn. Magn. Mater.* **2004**, *272–276*, 2003–2004.

(69) Singh, Y. Electrical Resistivity Measurements: A Review. *Int. J. Mod. Phys. Conf. Ser.* **2013**, *22*, 745–756.

(70) Singleton, J. *Band Theory and Electronic Properties of Solids*, 1st ed.; Oxford Matter Series in Physics, 2001.

For Tables of Contents Only
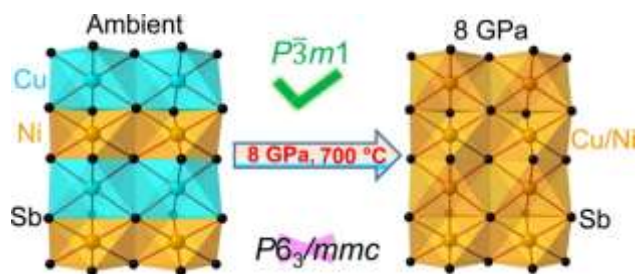
Mineral $CuNiSb_2$ was synthesized at ambient pressure and crystallized in the NiAs-derived structure ($P\bar{3}m1$, #164) with Cu and Ni ordering. The structure is constructed with Ni-Sb, Cu-Sb, and Cu-Ni bonding, and long weak Sb-Sb interactions. The high pressure sample prepared at 700 °C and 8 GPa adopts a disordered metal structure but still in the $P\bar{3}m1$ space group.

Ambient and High Pressure CuNiSb$_2$: Metal-Ordered and Metal-Disordered NiAs-Type Derivative Pnictides

Callista M. Skaggs,[1] Chang-Jong Kang,[2,#] Christopher J. Perez,[3] Joke Hadermann,[4] Thomas J. Emge,[5] Corey E. Frank,[5] Chongin Pak,[6] Saul H. Lapidus,[7] David Walker,[8] Gabriel Kotliar,[2] Susan M. Kauzlarich,[3] Xiaoyan Tan,*[1,5] and Martha Greenblatt*[,5]

[1]*Department of Chemistry and Biochemistry, George Mason University, Fairfax, Virginia 22030, United States*

[2]*Department of Physics and Astronomy, Rutgers, The State University of New Jersey, Piscataway, New Jersey, 08854, United States*

[3]*Department of Chemistry, University of California, Davis, California, 95616, United States*

[4]*EMAT, University of Antwerp, Groenenborgerlaan 171, B-2020 Antwerp, Belgium*

[5]*Department of Chemistry and Chemical Biology, Rutgers, The State University of New Jersey, Piscataway, New Jersey, 08854, United States*

[6]*Department of Chemistry and Biochemistry, Florida State University, Tallahassee, Florida, 32306, United States*

[7]*Advanced Photon Source, Argonne National Laboratory, Argonne, Illinois, 60439, United States*

[8]*Lamont Doherty Earth Observatory, Columbia University, Palisades, New York, 10964, United States*

Corresponding Authors* E-mail: xtan6@gmu.edu, greenbla@chem.rutgers.edu

Page

Table S1. Crystallographic data for CuNiSb$_2$ single crystal.

Empirical formula	Cu$_{0.95}$Ni$_{0.95}$Sb$_2$
Formula weight	359.64
Wavelength	0.71073 Å
Temperature	150 K
Crystal system	Trigonal
Trigonal	$P\bar{3}m1$
Unit cell dimensions	a = 3.9692(3) Å, c = 5.1297(5) Å, V= 69.989(2) Å^3
Volume	69.989(13) Å^3
Z	1
Density (calculated)	8.533 mg/m^3
Absorption coefficient	32.848 mm^{-1}
F(000)	159
Crystal size	0.10 x 0.06 x 0.04 mm^3
Theta range for data collection	3.972 to 53.848°.
Index ranges	-9<=h<=8, -9<=k<=8, -10<=l<=11
Reflections collected	2894
Independent reflections	353 [R(int) = 0.0439]
Completeness to theta = 25.242°	96.9 %
Absorption correction	Numerical
Max. and min. transmission	0.45926 and 0.20010
Refinement method	Full-matrix least-squares on F^2
Data / restraints / parameters	353 / 0 / 10
Goodness-of-fit on F^2	1.189
Final R indices [I>2sigma(I)]	R1 = 0.0218, wR2 = 0.0472
R indices (all data)	R1 = 0.0302, wR2 = 0.0609
Extinction coefficient	0.122(10)
Largest diff. peak and hole	1.337 and -1.361 e.Å^{-3}

Table **S2**. Atomic coordinates and equivalent isotropic displacement parameters ($\mathring{A}^2$x 10^3) and bond lengths [$\mathring{A}$] for CuNiSb$_2$ single crystal. U(eq) is defined as one third of the trace of the orthogonalized U$_{ij}$ tensor.

	x	y	z	U (eq)
Cu(1A)	0	0	0	7(1)
Ni(1B)	0	0	0	7(1)
Ni(1A)	0	0	0.5	7(1)
Cu(1B)	0	0	0.5	7(1)
Sb(1)	0.3333	0.6667	0.2530(1)	7(1)

Cu(1A)-Sb(1)#1 2.6337(2)   Ni(1A)-Sb(1)#6 2.6185(2)

Cu(1A)-Sb(1)#2 2.6337(2)   Ni(1A)-Sb(1)#3 2.6185(2)

Cu(1A)-Sb(1)#3 2.6337(2)   Ni(1A)-Sb(1)#7 2.6185(2)

Cu(1A)-Sb(1)   2.6337(2)   Ni(1A)-Sb(1)   2.6185(2)

Cu(1A)-Sb(1)#4 2.6337(2)   Ni(1A)-Sb(1)#4 2.6185(2)

Cu(1A)-Sb(1)#5 2.6337(2)   Ni(1A)-Sb(1)#8 2.6185(2)

Ni(1B)-Sb(1)#1 2.6337(2)   Cu(1B)-Sb(1)#6 2.6185(2)

Ni(1B)-Sb(1)#2 2.6337(2)   Cu(1B)-Sb(1)#3 2.6185(2)

Ni(1B)-Sb(1)#3 2.6337(2)   Cu(1B)-Sb(1)#7 2.6185(2)

Ni(1B)-Sb(1)   2.6337(2)   Cu(1B)-Sb(1)   2.6185(2)

Ni(1B)-Sb(1)#4 2.6337(2)   Cu(1B)-Sb(1)#4 2.6185(2)

Ni(1B)-Sb(1)#5 2.6337(2)   Cu(1B)-Sb(1)#8 2.6185(2)

Symmetry transformations used to generate equivalent atoms:

#1 -x,-y,-z   #2 -x+1,-y+1,-z   #3 x-1,y-1,z   #4 x,y-1,z   #5 -x,-y+1,-z   #6 -x+1,-y+1,-z+1

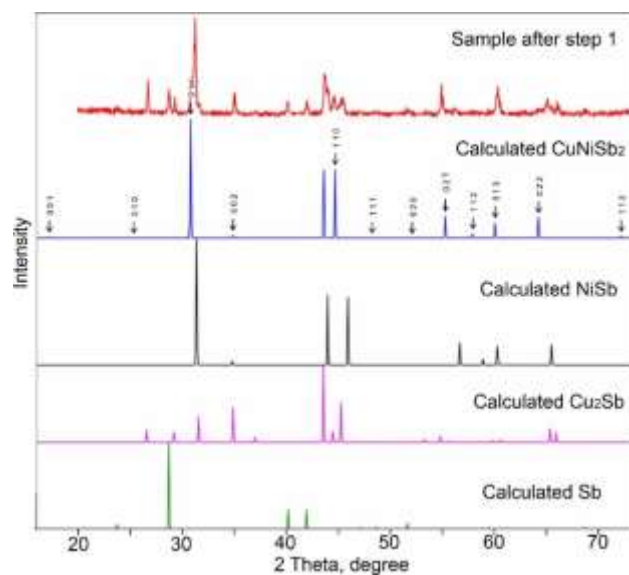#7 -x,-y,-z+1   #8 -x,-y+1,-z+1   #9 x,y+1,z   #10 x+1,y+1,z

Figure S1. Experimental PXD pattern of the sample annealed after the first annealing step (step 1), and comparisons with calculated patterns of $CuNiSb_2$, $NiSb$, Cu_2Sb, and Sb.
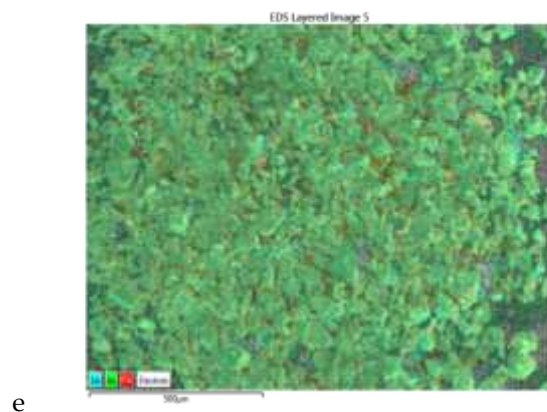

e

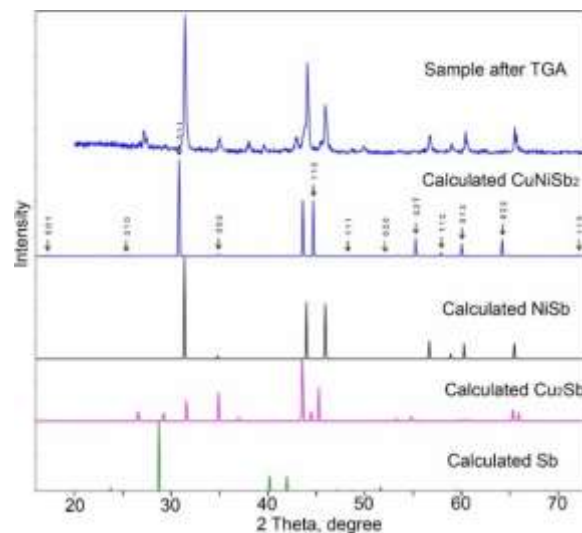Figure S2. The overall SEM and EDX elemental mapping of $CuNiSb_2$-AP particles.

Figure S3. Experimental PXD pattern of the sample after TGA-DSC experiment and calculated patterns of $CuNiSb_2$, NiSb, Cu_2Sb, and Sb.
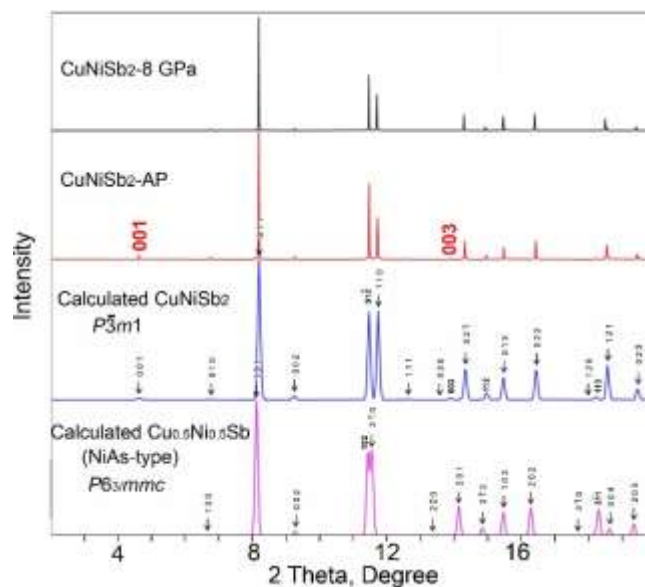

Figure S4. Experimental SPXD pattern of $CuNiSb_2$-8GPa and $CuNiSb_2$-AP, experiment and calculated patterns of $CuNiSb_2$ in the $P\bar{3}m1$ space group and calculated $Cu_{0.5}Ni_{0.5}Sb$ in the $P6_3/mmc$ space group.
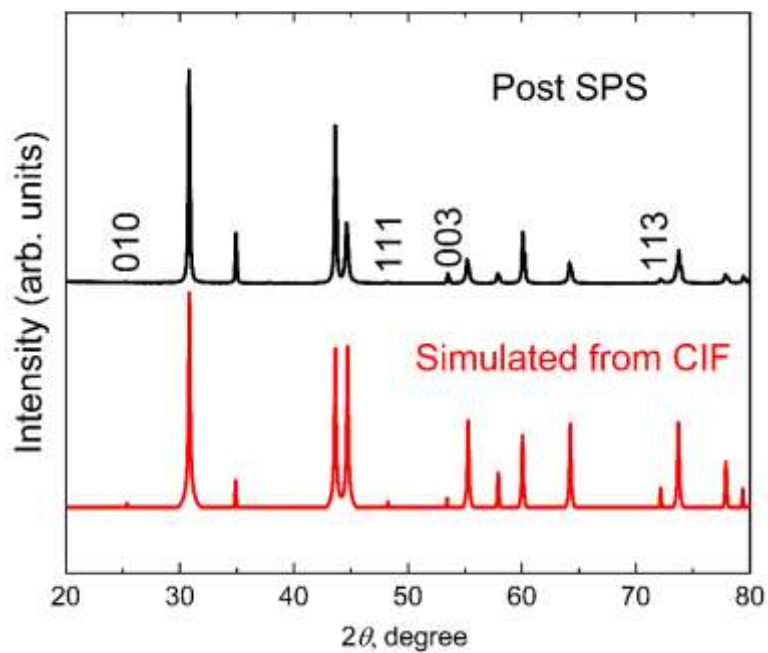
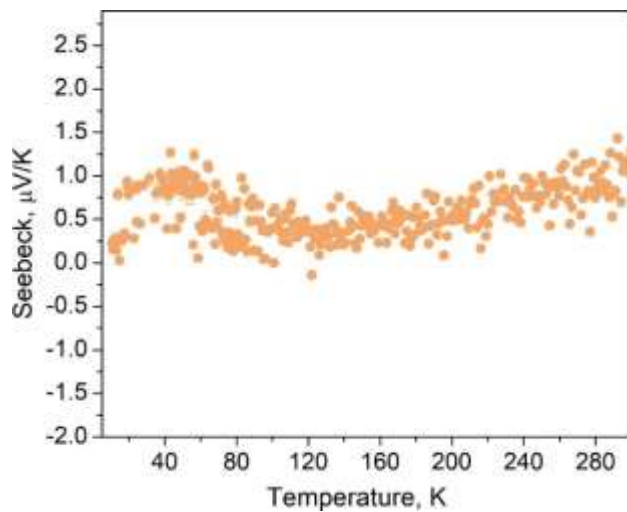Figure S5. Experimental PXD pattern of the dense pellet after SPS treatment.

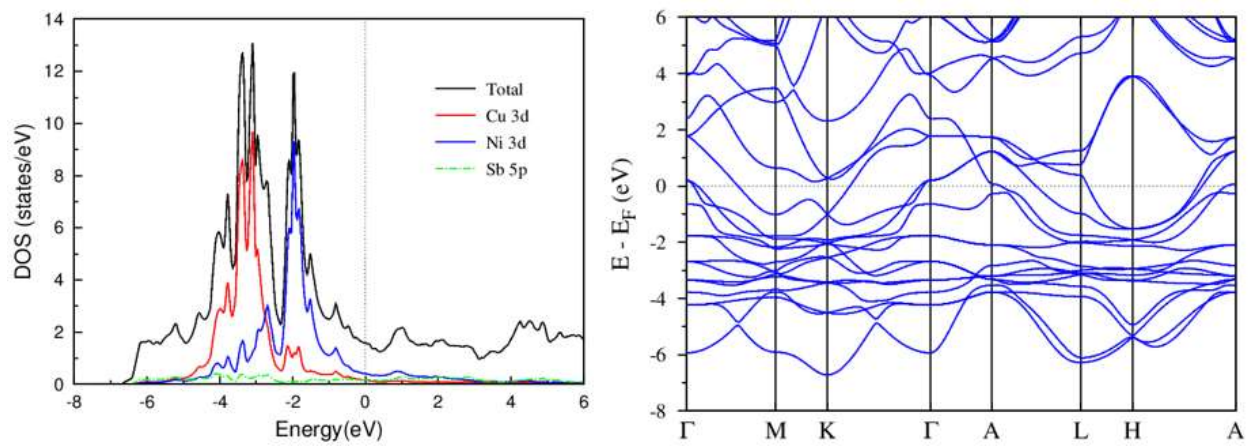Figure S6. Seebeck coefficient of $CuNiSb_2$-AP measured between 5 K and 300 K.

Figure S7. Density of states (DOS) and band structure of CuNiSb$_2$-AP using the WIEN2k software.